ADVANCED MATERIALS INTERFACES
Open Access
www.advmatinterfaces.de

Fe(III)-Mediated Formation of Cu Nanoinclusions and Local Heterojunctions in $CuWO_4$ Photoanodes

*Pietro Ostellari, Serge Benedoue, Diego Zamboni, Andrea Basagni, Sharon Silloni, Enrico Scattolin, Matteo Lorenzoni, Robertino Pilot, Ilaria Fortunati, Simone Lauciello, Mengjiao Wang, Mirko Prato, Julius N. Ndi, Francesca Arcudi, Luka Đorđević, Gaudenzio Meneghesso, Silvia Gross, Lorenzo Franco, Gian-andrea Rizzi, Teresa Gatti, and Francesco Lamberti**

Enhancing the photoelectrochemical (PEC) performance of $CuWO_4$ photoanodes has typically relied on doping or co-catalyst strategies to improve charge carrier dynamics. In this work, an alternative approach is presented in which Fe(III) acts as a self-assembly mediator during hydrothermal synthesis, enabling the formation of a core–shell heterostructure composed of a crystalline $CuWO_4$ core, a partially amorphous CuO/WO_3 shell, and embedded metallic Cu nanoinclusions. Rather than functioning as a dopant or co-catalyst, Fe(III) is completely removed during post-synthetic treatment, mediating a redox-guided phase reorganization without being incorporated into the final material. This architecture establishes local heterojunctions that facilitate charge separation, suppress recombination, and enhance oxygen evolution reaction (OER) activity. A relative increase of ≈30-fold in photocurrent is observed compared to pristine $CuWO_4$, as confirmed by structural, spectroscopic, and electrochemical analyses. While absolute photocurrents remain modest, this enhancement reflects intrinsic modifications in charge transport and recombination behavior driven by Fe(III)-mediated structural reorganization. Complementary photocatalytic dye degradation experiments reveal that Fe-activated particles act as highly efficient ROS-generating catalysts in suspension, demonstrating functionality beyond thin-film devices. These findings offer a new paradigm for oxide photoanode design, leveraging Fe(III)-induced self-assembly to engineer multifunctional heterostructures without relying on conventional doping.

1. Introduction

Doping strategies are commonly employed to enhance charge separation and improve the photocurrent response of semiconductor photoanodes in solar-driven water splitting applications.[1–10] In the case of $CuWO_4$—a chemically stable and visible-light-responsive oxide[11–13] transition metal doping has been widely explored to address its intrinsic limitations, including poor carrier mobility and high bulk recombination rates.[14–18] Indeed, dopants such as fluorine,[19] molybdenum,[20] nickel,[21] yttrium,[22] and vanadium[23] have been shown to moderately shift band positions or introduce shallow defect levels, thereby improving photoelectrochemical (PEC) performance to some extent.

Among potential dopants, Fe^{3+} has garnered significant attention due to its redox versatility and compatibility with copper-based oxides.[24,25] Several studies have reported performance enhancements in Fe-modified $CuWO_4$,

P. Ostellari, S. Benedoue, D. Zamboni, A. Basagni, S. Silloni, E. Scattolin, R. Pilot, I. Fortunati, F. Arcudi, L. Đorđević, S. Gross, L. Franco, G.-a. Rizzi, F. Lamberti
Department of Chemical Sciences
University of Padova
Via Marzolo 1, Padova 35131, Italy
E-mail: Francesco.lamberti@unipd.it

The ORCID identification number(s) for the author(s) of this article can be found under https://doi.org/10.1002/admi.202500610

DOI: 10.1002/admi.202500610

S. Benedoue, J. N. Ndi
Applied Physical and Analytical Chemistry Laboratory
Department of Inorganic Chemistry
Faculty of Science
University of Yaoundé 1
P.O. Box 812, Yaoundé BP 812, Cameroon

M. Lorenzoni, S. Lauciello, M. Prato
Material Characterization Facility
Italian Institute of Technology (IIT)
Via Morego 30, Genova 16163, Italy

S. Gross, T. Gatti, F. Lamberti
National Interuniversity Consortium of Materials Science and Technology (INSTM)
Florence 50121, Italy

interpreting these results as evidence of successful Fe doping.[26,27] Notably, Lhermitte and Bartlett[13] proposed that the enhanced performance observed in Fe-treated $CuWO_4$ may arise from the formation of WO_3-rich domains rather than from true lattice doping, suggesting that the presence of Fe^{3+} might facilitate phase segregation rather than provide direct electronic benefits.

In this work, we effectively demonstrate that under hydrothermal synthesis conditions, Fe^{3+} does not substitute into the $CuWO_4$ lattice. Instead, it operates as a self-assembly mediator, orchestrating redox restructuring and local phase segregation, as suggested by Lhermitte and Bartlett in their account paper cited above. This Fe-driven process leads to the formation of a complex heterostructure composed of a crystalline $CuWO_4$ core, an amorphous/crystalline CuO/WO_3 shell, and metallic Cu nanoinclusions. This multiphase architecture substantially improves both PEC and photocatalytic performance, even though Fe is entirely absent in the final material.

This finding challenges the prevailing assumption that enhanced performance originates from direct Fe doping. Rather, our results point to transient Fe-induced structural modulation as the primary mechanism—bypassing many of the long-term stability issues and defect-related drawbacks associated with traditional doping.[28–31] Compositional and spectroscopic analyses, including UV-Vis of washing solutions, X-ray photoelectron spectroscopy (XPS), and energy-dispersive X-ray spectroscopy (EDX), confirm the complete removal of Fe after synthesis and calcination.

Building on this evidence, we propose a mechanistic hypothesis in which Fe^{3+} triggers a cascade of redox reactions during hydrothermal processing, facilitating the spontaneous formation of nanoscale pn heterojunctions. Although additional in situ studies will be necessary to verify intermediate steps, our data consistently support the role of Fe^{3+} as a non-incorporated structural mediator rather than a dopant or co-catalyst. This approach opens new avenues for designing multifunctional photoanodes and ROS-generating photocatalysts through Fe-mediated heterostructure engineering—without the need for permanent chemical doping.

M. Wang, T. Gatti
Department of Applied Science and Technology
Politecnico di Torino
Corso Duca degli Abruzzi 24, Torino 10129, Italy
G. Meneghesso, F. Lamberti
Department of Industrial Engineering
University of Padova
Via Gradenigo 6a, Padova 35131, Italy
S. Gross
Karlsruher Institut für Technologie (KIT)
Institut für Technische Chemie und Polymerchemie (ITCP)
Engesserstr. 20, 76131 Karlsruhe, Germany
T. Gatti
Center for Materials Research
Justus Liebig University
Heinrich-Buff-Ring 17, 35392 Giessen, Germany
F. Lamberti
Zhejiang Beisheng Photovoltaic Co. Ltd.
No 800 Zhenbei Road, Wuxing, Huzhou, Zhejiang 313000, China

2. Results and Discussion

The pristine $CuWO_4$ nanopowder was synthesized following the procedure detailed in the Experimental Section, utilizing a subcritical hydrothermal approach. To assess the influence of Fe(III) during synthesis, a stoichiometric amount of ferric nitrate was introduced, achieving a nominal Fe/Cu molar ratio of 0.8 at% and 1.6 at% (**Figure 1**). These values were selected based on preliminary trials (detailed in the Supporting Information) as the maximum levels that allowed retention of the $CuWO_4$ structure, essential for PEC activity. The resulting powders were successfully dispersed in an isopropyl alcohol (IPA) mixture at 0.5 g L^{-1}, as described in the Experimental Section. The thin films—designated as $CuWO_4$ (pristine), Fe@$CuWO_4$ 0.8%, and Fe@$CuWO_4$ 1.6% (corresponding to the lower and higher Fe content in the precursor solution, respectively)—were fabricated via an ultrasonic spray-coating system (Figure 1f) and employed as photoanodes for PEC OER measurements using chopped linear sweep voltammetry.

The electrochemical characterization (**Figure 2a**) reveals a clear enhancement in photocurrent for Fe-treated samples. At 1.23 V versus RHE, the photocurrent increases from 1 μA cm^{-2} for pristine $CuWO_4$ to 6.7 μA cm^{-2} for Fe@$CuWO_4$ 0.8% and 27.8 μA cm^{-2} for Fe@$CuWO_4$ 1.6%, corresponding to a ≈ 30-fold increase. While absolute values remain in the tens of μA cm^{-2}—typical for $CuWO_4$-based photoanodes without catalytic overlayers and of submicrometer thicknesses[13,32] this result highlights the effectiveness of the Fe-mediated structural modification. Importantly, no co-catalysts were employed in this study, unlike prior works where photocurrent enhancements were achieved through deposition of catalytic layers such as NiFeOx or Co-Pi.[14,33] This choice was intentional, aimed at isolating the intrinsic contribution of Fe(III) to the formation of active heterostructures without interference from external catalytic effects. However, these results are in apparent agreement with previous literature that attributed similar enhancements to Fe doping.[26,34] Similarly, EDX and XPS on pristine and Fe-treated samples (Figures S3,S4, and S7–S9, Supporting Information) do not show any evidence of the presence of iron inside the structure confirming existing literature. However, we aim at better understanding the fate of the iron during the synthesis processes. To identify the compositional window in which it may influence material properties, we conducted a dedicated investigation combining structural and optical characterization. In particular, the powders were washed three times with 0.5 M HCl (total 15 mL), twice with deionized water and once with isopropanol to remove excess water; then, the samples were dried in oven at 80 °C overnight. The mother liquors obtained after the washing with HCl were kept and analyzed with UV–vis, thus assessing the presence of Cu^{2+} or Fe^{3+} leached from the samples.

In Figure 2b the UV–vis spectra are reported. From the UV-Vis spectra of the samples, only the pristine sample showed an evident peak around 810 nm relative to Cu^{2+}, indicating that probably the CuO formed during the annealing of the powder was leached with HCl. The Fe@$CuWO_4$ samples showed only a weak peak at 810 nm, indicating that very few copper was leached from the powders. Despite this, the most interesting aspect is the shoulder in the absorption spectra of the Fe@$CuWO_4$ samples (inset Figure 2b) at 330 nm indicating the presence of Fe^{3+}

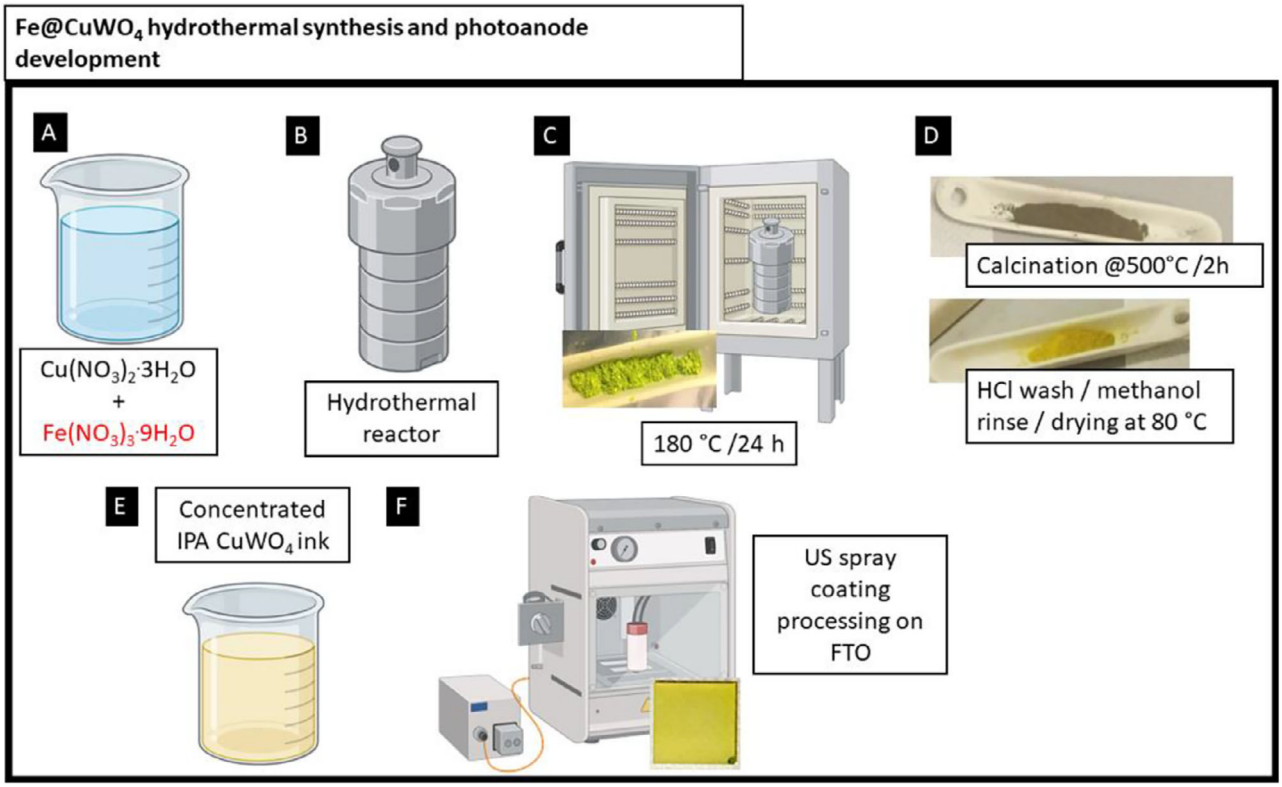

Figure 1. Sketch representing the step-by-step synthesis of activated and pristine $CuWO_4$ nanopowders. The precursors are dissolved in a beaker (a), then transferred to an autoclave (b), followed by thermal treatment in oven (c) and further purification steps (d). The $CuWO_4$ ink is then prepared in IPA (e) and the photoanode is finally obtained by US spray coating on FTO (f). Optical images of produced nanopowders and $CuWO_4$ films. Figure created using BioRender.com with author modifications.

in solution.[35] This finding suggests that iron likely did not enter the crystal structure of $CuWO_4$ and was leached during the washing step with HCl. To validate this interpretation quantitatively, we performed inductively coupled plasma optical emission spectroscopy (ICP-OES) on the dried powders (Figure 2c). While the nominal Fe precursor concentrations were 0.8%, 1.6%, and 3.2% atomic, the corresponding Fe contents in the final powders were found to be 0.032%, 0.064%, and 0.78% at%, respectively. The first two values fall below the typical detection limit of EDX and confirm the absence of any significant Fe incorporation. The third sample (nominal 3.2%) exhibits a measurable amount of Fe but also shows extensive WO_3 segregation (as discussed below), making it unsuitable for further analysis. Therefore, we conservatively define 1.6% nominal Fe as the practical upper limit for our system—above which structural disruption outweighs any beneficial effects.

To assess the formation of crystalline $CuWO_4$ after the annealing process, we recorded the X-ray diffraction pattern of the samples, as reported in Figure 2d. The search-and-match analysis of the XRD pattern of the pristine sample identified $CuWO_4$ as the only crystalline phase, confirming that annealing followed by an acid wash effectively promoted $CuWO_4$ formation and removed excess CuO. The XRD patterns of the powders obtained after hydrothermal treatment revealed the presence of crystalline WO_{3-x} phases along with an amorphous contribution, likely attributable to amorphous $CuWO_4$, as no other copper-containing phases were detected.[36–40] Accordingly, the identification of a pure $CuWO_4$ phase in the pristine sample suggests that the amorphous $CuWO_4$ was quantitatively transformed into a crystalline phase. In contrast, the Fe@$CuWO_4$ samples exhibited both $CuWO_4$ and WO_3 after calcination, as shown in Figure 2e. The introduction of Fe^{3+} into the reaction mixture reduced the amount of copper available for $CuWO_4$ formation, leading to a substoichiometric Cu content relative to tungstate. As a result, the excess tungstate, unable to be fully incorporated into the $CuWO_4$ structure, precipitated separately as WO_3. Moreover, the amount of WO_3 in Fe@$CuWO_4$ increased with the iron content in the reaction mixture, yet no iron-containing crystalline phases were detected.

As said, since the Fe@$CuWO_4$ 3.2% sample contained a significant amount of WO_3 relative to $CuWO_4$, we decided to exclude it from further analysis. Despite the negligible Fe incorporation confirmed by ICP-OES, we defined 1.6% nominal Fe as the practical upper limit, since higher precursor concentrations result in increased WO_3 segregation.

As demonstrated in the dedicated Supporting Results (Figures S16 and S17, Supporting Information), Fe^{3+} is completely removed after synthesis and calcination, even under conditions specifically designed to promote substitution. UV-Vis analysis of the washing solution and structural comparisons with Fe-enriched reference samples confirm that Fe does not incorporate into the $CuWO_4$ lattice (Figure 2b,c). Therefore, the observed

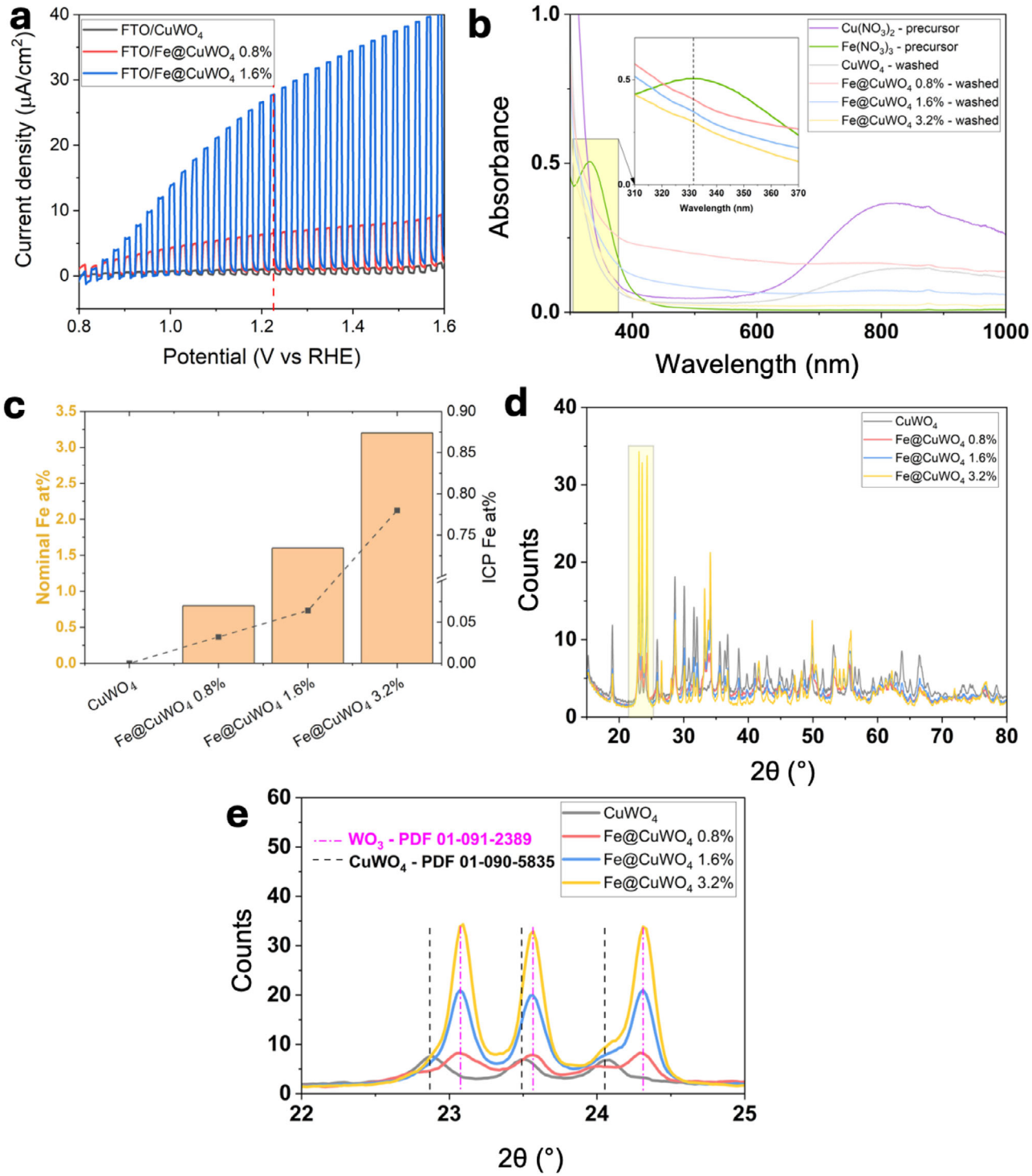

Figure 2. a) Linear sweep voltammetry (LSV) under chopped visible light illumination for pristine $CuWO_4$ and Fe-treated samples (0.8% and 1.6%). A progressive photocurrent enhancement is observed with increasing Fe precursor concentration. b) UV–vis absorbance spectra of washed powders after synthesis, including $CuWO_4$ and $Fe@CuWO_4$ with 0.8%, 1.6%, and 3.2% nominal Fe content. The inset highlights the 310–370 nm region, suggesting slight band edge modulation consistent with shell formation. c) Correlation between nominal Fe content in the synthesis precursor (orange bars, left axis) and measured Fe content in the final materials by ICP-OES (black squares, right axis). ICP values reveal residual Fe levels of only 0.032, 0.064, and 0.78 at% for the 0.8%, 1.6%, and 3.2% Fe-treated samples, respectively, confirming minimal incorporation of Fe^{3+} into the final product. d) XRD patterns of $CuWO_4$ and $Fe@CuWO_4$ samples. The grey line shows the pristine reference; Fe-treated samples reveal additional peaks due to WO_3. e) Zoomed-in view of the (110)/(011) region, highlighting progressive peak shifts and shoulder formation indicative of WO_3 segregation with increasing Fe content.

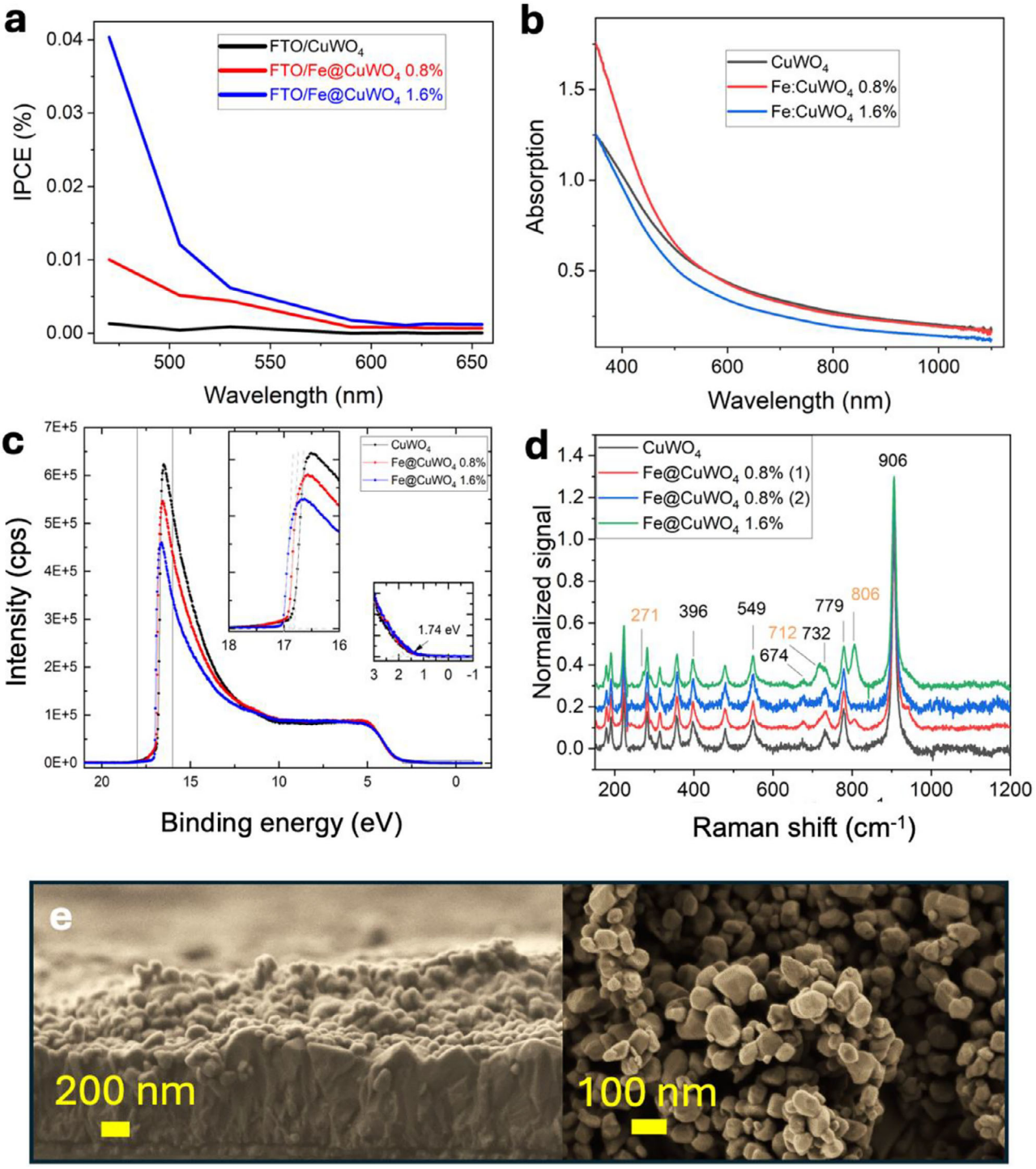

Figure 3. a) IPCE for the different photoanodes at 1.23 V versus RHE; b) UV–vis spectra; c) UPS analysis of the samples; d) Raman spectra (two different areas for $CuWO_4$ 0.8% sample were collected showing not uniform distribution on the sample) and e) cross sectional and top view SEM images of Fe@$CuWO_4$ 1.6%.

improvements in photocurrent must instead be attributed to Fe-mediated structural reorganization, rather than classical doping mechanisms.

The incident photon-to-current efficiency (IPCE) analysis further supports these observations (**Figure** 3a), revealing a pronounced increase in conversion efficiency within the blue-green spectral region (450–550 nm), which aligns with the material's optical bandgap. This indicates that the treated samples exhibit improved photoresponse in a spectral range critical for OER performance. While the exact mechanism behind this

enhancement requires further investigation, the data suggest that Fe(III) facilitates structural modifications leading to enhanced charge separation.

Given these results, one possible explanation is that the Fe(III)-mediated synthesis leads to a reorganization of the $CuWO_4$ structure, reducing excitonic recombination and improving charge carrier mobility. This hypothesis aligns with the observed photocurrent trends but requires additional analysis to distinguish whether these effects arise from phase segregation, band structure realignment, or modifications to interfacial charge transfer pathways.

Given the remarkable photocurrent enhancement observed in Fe(III)-treated $CuWO_4$ samples, we focused on understanding the microscopic origins of this improvement by thoroughly investigating the optical, morphological, and electrical properties of the photoanodes. Since Fe(III) is entirely removed after synthesis, the observed performance enhancement must originate from structural and morphological modifications rather than from Fe incorporation.

To elucidate potential structural and electronic modifications, we first examined the elemental composition and microstructural features of the films. The UV-Vis-NIR absorption spectra of the different photoanodes are presented in Figure 3b, displaying the characteristic absorption profile of $CuWO_4$, with a gradual increase in absorption near 500 nm, corresponding to its indirect bandgap. This optical response is consistent with the IPCE trends, reinforcing the correlation between the band structure and photoelectrochemical activity. The Cody plot analysis[41] (Figure S6a, Supporting Information) reveals an indirect optical bandgap of ≈2.1–2.2 eV for all samples, with a slight blue shift (≈0.1 eV) observed for Fe(III)-treated films. This shift, albeit minor, aligns with literature-reported values for $CuWO_4$[14] and suggests subtle modifications in the electronic structure. Additionally, the near-infrared (NIR) region of the spectra shows a noticeable reduction in light scattering, particularly for Fe@$CuWO_4$ 1.6%. This implies a smoother surface morphology, which is further supported by atomic force microscopy (AFM) roughness analysis (Figure S1, Supporting Information). The measured average roughness values were (170 ± 18) nm for pristine $CuWO_4$, (160 ± 18) nm for Fe@$CuWO_4$ 0.8%, and (145 ± 18) nm for Fe@$CuWO_4$ 1.6%, indicating a systematic reduction in surface irregularities upon Fe(III)-mediated processing.

The morphological evolution of the films was further examined through scanning electron microscopy (SEM). The SEM images of the Fe@$CuWO_4$ 1.6% sample (Figure 3g) reveal a submicrometer-thick film with rounded grains assembled into a 3D structure. The cross-sectional SEM analysis confirms that $CuWO_4$ exhibits a granular, polyhedral morphology, with individual particles forming loosely packed agglomerates. The presence of valleys and nanometric voids indicates incomplete packing, leading to regions of lower particle density where the fluorine-doped tin oxide (FTO) substrate remains partially exposed. This structural feature may contribute to the overall low absolute photocurrent values observed for all samples, as incomplete film coverage can lead to charge loss at the electrode interface.

The nano-crystalline nature of $CuWO_4$ grains is clearly observed, resembling structures reported for sonochemical methods followed by furnace treatments at 500 °C.[42] This confirms that our hydrothermal synthesis effectively produces nanoscale $CuWO_4$ particles suitable for thin-film fabrication.

SEM analysis (Figure S2, Supporting Information) reveals a similar morphology across all samples, with a non-compact film structure attributed to suboptimal nanopowder deposition. This differs from denser films obtained via spray pyrolysis, electrochemical deposition, or hydrothermal direct growth.[43–45] Future efforts will focus on optimizing deposition conditions to enhance uniformity and coverage.

To further investigate the elemental composition, energy dispersive X-ray (EDX) characterization was performed on the dispersed nanopowders (Figure S3, Supporting Information). This analysis was conducted to enable a semi-quantitative detection of iron within the powder. However, no detectable iron was found in any sample, consistent with previous studies on Fe^{3+}-doped $CuWO_4$ photoanodes.[26,34] While these reports have attributed the absence of an Fe signal to the low dopant concentration, we take a more conservative and data-driven approach, refraining from asserting any Fe incorporation within the samples. Furthermore, post-synthetic washing steps and calcination (see Supporting Results) are likely responsible for the complete removal of residual Fe species, supporting the conclusion that Fe(III) does not persist in the final material corroborating EDX analyses (Figures S7–S9, Supporting Information).

The material characterization aims to elucidate the effect of Fe(III)-mediated synthesis on the electronic structure and phase composition of $CuWO_4$. UPS analysis (Figure 3c) indicates a slight n-doping effect, evidenced by a reduction in the work function from 4.4 eV (pristine $CuWO_4$) to 4.2 eV (Fe@$CuWO_4$ 1.6%), which suggests the formation of shallow defect states. This shift, while subtle, aligns with structural modifications induced by Fe(III) during synthesis rather than direct doping effects. Further supporting this interpretation, XPS spectra (Figure S4, Supporting Information) confirm the absence of Fe signatures in the Cu 2p and W 4f regions, reinforcing the conclusion that Fe is not effectively incorporated into $CuWO_4$. Additionally, the valence band maximum (VBM) remains at 1.7 eV below the Fermi level for all samples, consistent with literature values for $CuWO_4$.

To assess potential structural modifications, Raman analyses on thin films (Figure 3d) were performed. These data reveal the emergence of a WO_3 phase in Fe-treated samples, with an increasing trend corresponding to Fe concentration. Raman spectra show additional peaks at 271, 712, and 806 cm^{-1}, which are characteristic of WO_3, while the $CuWO_4$ vibrational modes remain unchanged. Quantitative analysis through Pawley–Rietveld refinement (Figure S6, Supporting Information) of the XRD reported in Figure 2 reveals an increase in WO_3 content from <1 wt.% to over 6 wt.% in Fe-treated samples, while CuO content remains constant at ≈1 wt.%. These findings clearly indicate that Fe(III) promotes phase segregation, leading to the formation of a multiphase heterostructure rather than acting as a dopant. Additional experiments (Figure S17, Supporting Information) show that WO_{3-x} domains already form prior to full calcination, further confirming that the phase separation is initiated during hydrothermal synthesis and not driven by post-annealing rearrangements. This supports the role of Fe(III) as a self-assembly mediator guiding early-stage oxide reorganization. The presence of WO_3 and CuO phases supports the formation of a composite structure, contributing to band

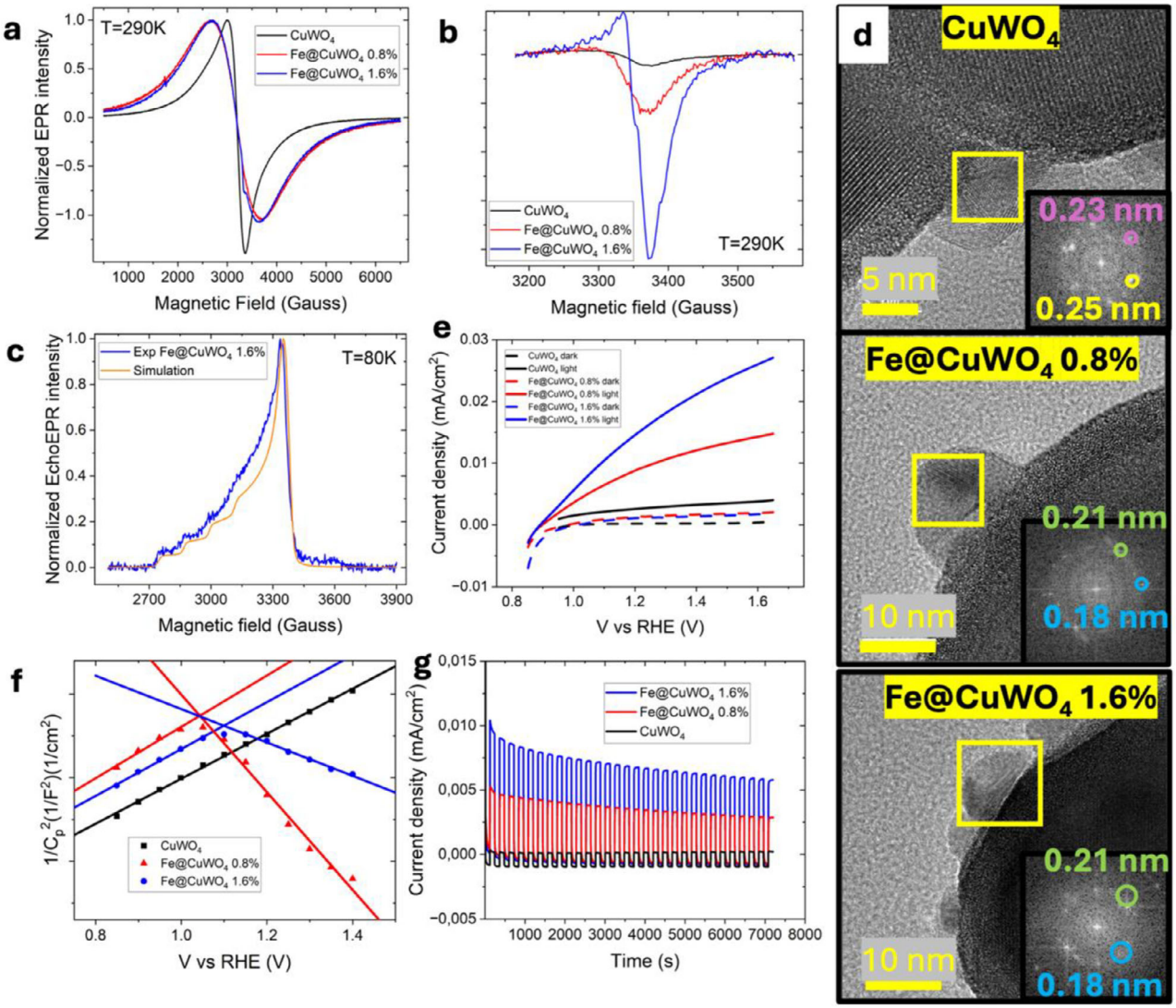

Figure 4. a) EPR analysis of the different $CuWO_4$ photoanodes and b) relative zoom in the 3300–3400 Gauss region; c) EchoEPR of the Fe@$CuWO_4$ 1.6% sample with overlayed simulated curve; d) HR-TEM analysis of the different samples (inset plots represent the FT analysis of the squared area); e) LSV for the different samples in dark and light conditions; f) Mott-Schottky plot; g) Chronoamperometry in chopped light for long-term analysis.

realignment and an upshift of the valence band due to localized n-doping effects. The interaction between $CuWO_4$, CuO, and WO_3 (Figure S5, Supporting Information) plays a key role in modifying the electronic landscape, improving charge separation, and enhancing PEC performance. For a more detailed discussion on Raman, UPS, and KPM analyses, refer to the Supporting Information.

Given the evidence of multiphase features in Fe-treated samples, we investigated the outer shell composition to understand its contribution to the enhanced OER activity. CuO, a low-bandgap p-type semiconductor prone to oxygen deficiencies, is known to facilitate hole transfer for water oxidation.[46] To probe the chemical nature of this shell and its possible catalytic function, we employed electron paramagnetic resonance (EPR) spectroscopy, exploiting the paramagnetic character of Cu(II) (d^9). Additionally, EPR is sensitive to oxygen vacancies, a key factor in the photocatalytic activity of transition metal oxides.[47] Room-temperature EPR spectra (**Figure** 4a) show broad Lorentzian signals for all samples, indicating strong exchange interactions among Cu(II) centers. The Fe-treated samples display a broader linewidth (1750 G) compared to pristine $CuWO_4$ (1550 G), suggesting increased lattice disorder and formation of shallow electronic defect states. A weaker signal at B ≈ 3350 G (g ≈ 2.06), visible only in the Fe-treated samples (Figure 4b), corresponds to isolated Cu(II) sites—likely distorted surface or bulk centers where exchange interactions are suppressed.[48] Low-temperature pulsed EPR (80 K, Figure 4c) confirms the presence of axially symmetric Cu(II) sites in Fe@$CuWO_4$ 1.6%. The simulation, based on spin Hamiltonian parameters (Table S1, Supporting Information), suggests local coordination with oxygen, with no hyperfine interactions involving other spin-active nuclei (e.g., ^1H or ^{183}W). These findings support the hypothesis that Fe

treatment promotes the formation of non-crystallographic Cu(II) sites.

To correlate these observations with the structural morphology, we conducted TEM analysis on both pristine and Fe-treated samples (Figure 4d). While both show similar nanoparticle distributions (tens of nm in size), two key differences emerge in Fe-treated materials: i) formation of a core-shell structure, with a crystalline $CuWO_4$ core and an amorphous 5–10 nm thick shell decorated with small semi-crystalline protrusions; ii) a compositional shift in these protrusions, which appear CuO-like in pristine samples but exhibit Cu^0-like character in Fe-treated ones. TEM and SAED allow identification of the core as $CuWO_4$, while the amorphous shell contains WO_3 and Cu-based oxides, in agreement with Raman and XRD data.

In pristine samples, HRTEM reveals lattice fringes at 2.5 and 2.3 Å, attributed to CuO ((−111) and (111) planes, PDF 01-073-6234). In Fe-treated samples, these shift to 2.1 and 1.8 Å, matching Cu ((111) and (200) planes, PDF 03-065-9026), suggesting the formation of metallic Cu nanoinclusions. EDX analysis of the protrusions (Figure S10, Supporting Information) further supports this structural evolution, showing an increase in the Cu/O ratio from ≈1:1 in pristine samples to 3:1–5:1 in Fe-treated ones. Among these, the 1.6% Fe sample exhibits the most favorable distribution of Cu^0 domains, while maintaining the core–shell heterostructure. The 3.2% Fe sample, described in the Supporting Results (Figure S17, Supporting Information), shows a greater relative intensity of WO_3 reflections in XRD, suggesting a shift in the overall phase balance. Although a systematic increase in metallic Cu content with Fe concentration is not discernible from bulk characterization, HRTEM suggests a localized enrichment of Cu^0 at higher Fe loadings. Overall, the combination of high-resolution imaging and semi-quantitative EDX analysis indicates that the shell region consists of a mixed WO_3-rich matrix containing dispersed CuxO and metallic Cu domains. Although the spatial resolution of EDX limits precise interface definition, the consistent differences in contrast and local composition support the assignment of a heterogeneous shell structure beyond pure Cu enrichment. Based on these findings, 1.6% Fe was selected as the optimal concentration.

The presence of non-stoichiometric Cu(II) centers inferred from EPR aligns with the amorphous CuO/WO_3 shell observed in TEM. A line profile analysis by EDX (Figure S11, Supporting Information) shows that in the pristine sample, Cu and W contents are similar within the amorphous region, suggesting an amorphous $CuWO_4$-like composition. In contrast, Fe-treated samples exhibit lower Cu content relative to W in the shell, pointing to the presence of isolated Cu(II) centers within a WO_3-rich matrix.

Although TEM/EDX cannot definitively quantify Cu oxidation states, EPR strongly indicates that Fe activation promotes formation of reactive Cu(II) sites. These are considered catalytically relevant due to their defective environment and high redox activity, potentially enhancing charge transfer dynamics.[49]

The coexistence of CuO and WO_3 in the amorphous shell, along with the emergence of Cu^0-like inclusions, suggests the formation of interfacial heterojunctions. While further analysis is needed, these structural features likely contribute to enhanced charge separation and transport, underpinning the superior PEC performance observed.

To assess the correlation between the nanostructure and PEC behavior, we conducted advanced electrochemical measurements. Linear sweep voltammetry (LSV) under dark and illuminated conditions (Figure 4e) shows that Fe-treated $CuWO_4$ samples exhibit a clear enhancement in PEC activity compared to the pristine material. In particular, the onset of the photocurrent shifts by ≈100 mV toward lower potentials—from 0.95 to 0.85 V versus RHE—indicating a reduced overpotential for the oxygen evolution reaction (OER). While this trend is consistent with a beneficial structural or electronic modification induced by Fe treatment, the mechanistic origin of this improvement is not yet fully clarified at this stage. To rationalize these effects, we now turn to a more detailed electrochemical investigation—including Mott–Schottky analysis and intensity-modulated photocurrent spectroscopy (IMPS)—in order to elucidate the changes in band structure, charge transport, and recombination kinetics associated with the Fe-mediated nanostructuring.

Therefore, further insights into the electronic behavior were obtained from Mott-Schottky analysis (Figure 4f), with capacitance values (Cp) extracted from EIS data (Figure S12, Supporting Information).[50] The pristine $CuWO_4$ shows a typical n-type semiconductor profile, with a positive slope. In contrast, Fe-treated samples exhibit a nonlinear response with slope inversion, characteristic of a *pn* junction. This suggests the formation of a built-in electric field in Fe-activated samples, likely originating from the core-shell architecture and multiphase heterojunctions, which facilitates charge carrier separation. Interestingly, the flat band potentials of both pristine and Fe-treated samples are similar, ranging from 0.24 to 0.37 V versus RHE—well below the OER thermodynamic threshold (1.23 V). This implies that the enhanced activity is not due to a shift in flat band potential, but rather to improved interfacial charge transfer and reduced recombination losses. Supporting this, the electrochemical surface area (ECSA) remains nearly constant across all samples (Figure S13a, Supporting Information), excluding increased surface area as the dominant factor. Finally, the stability of PEC performance was assessed by running LSV under illumination for 2 h (Figure 4g). The Fe-treated samples maintain a stable photocurrent with minimal degradation, indicating that the engineered heterostructure not only improves performance but also sustains long-term photoactivity and structural integrity.

The electrochemical findings are further supported by photoluminescence (PL) analysis. Treated samples exhibit pronounced PL quenching (Figure S13b, Supporting Information), indicating reduced radiative recombination and suggesting more efficient charge separation and extraction upon Fe activation. This behavior aligns with the improved photocurrent and lower overpotentials observed previously.

To gain deeper insights into the charge transfer and recombination dynamics, we performed IMPS on both pristine and Fe@$CuWO_4$ 1.6% samples. IMPS Nyquist plots reveal striking differences: the pristine sample shows potential-independent semicircles (**Figure 5**a; Figure S14a, Supporting Information), indicating minimal modulation of charge transfer resistance. This suggests that charge carrier dynamics in pristine $CuWO_4$ are not effectively influenced by the applied bias, likely due to limited internal electric fields and inefficient carrier separation. In contrast, Fe-treated samples display a strong potential dependence (Figure 5a; Figure S14b, Supporting Information), with the

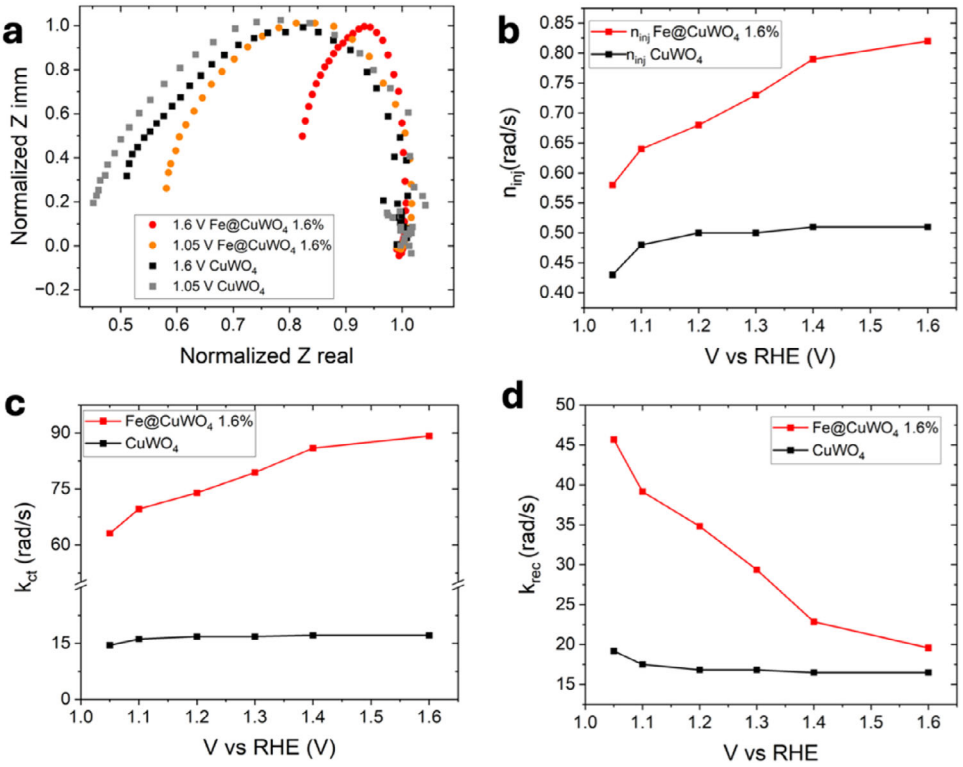

Figure 5. a) IMPS analysis for pristine and Fe@CuWO4 1.6% samples; b) charge injection, c) charge transfer, and d) recombination time constants behavior with applied potential; e) Sketch representing the suggested mechanism of Fe-activated $CuWO_4$ mediated OER. A process refers to OER path, whereas process B to electron-hole recombination.

semicircle size decreasing as the potential increases. This trend implies that Fe activation enhances band bending and internal electric fields, promoting more efficient charge extraction and transport under applied bias. Time-resolved analysis of the IMPS data (Figure 5b–d) provides further support. For Fe@$CuWO_4$ 1.6%, both the injection rate (n_{inj}) and charge transfer rate (k_{CT}) increase with applied potential, indicating improved kinetics for carrier injection and interfacial transfer. In contrast, these parameters remain essentially constant in the pristine sample, reinforcing the idea of limited responsiveness to external bias. The recombination rate (k_{rec}) also decreases more rapidly in the Fe-treated sample, although its higher values at elevated potentials suggest a larger carrier population due to more efficient injection.

Taken together, these results highlight the functional significance of the Cu nano-inclusions observed via TEM in Fe-activated samples. These inclusions likely serve as active catalytic sites and also contribute to the formation of a pn junction, as supported by Mott-Schottky analysis. Their presence enhances charge separation and directional transport, leading to lower overpotentials (LSV), built-in electric fields (Mott-Schottky) and bias-responsive charge dynamics (IMPS).

The combined structural and electronic modifications introduced by Fe(III)—despite its absence in the final material—enable a synergistic improvement in OER performance, validating the self-assembly mediator role of iron in $CuWO_4$ nanostructuring.

In light of the observed structural differences between pristine and Fe-activated $CuWO_4$, we propose a plausible mechanistic pathway to rationalize the formation of metallic Cu, amorphous CuO, and WO_3 in the Fe-treated samples. All syntheses were performed at pH 10, adjusted by ammonia addition. Under these conditions, Cu^{2+} may form $[Cu(NH_3)_x]^{2+}$ complexes or precipitate as $Cu(OH)_2$, while tungstate remains present as WO_4^{2-}. In the pristine synthesis, these react to form $CuWO_4$ directly:[42]

$$Cu^{2+}_{(aq)} + WO^{2-}_{4(aq)} \rightarrow CuWO_{4\,(s)} \quad (1)$$

Upon calcination at 500 °C, partial decomposition yields CuO and WO_3:

$$CuWO_{4(s)} \underset{500\,^\circ C}{\rightarrow} CuO_{(s)} + WO_{3(s)} \quad (2)$$

However, when Fe^{3+} is introduced forcing the doping to be substitutional, the mechanism diverges. At high pH, Fe^{3+} readily precipitates as FeOOH:[51]

$$Fe^{3+}_{(aq)} + 2OH^{-}_{(aq)} \rightarrow FeOOH_{(s)} + H^{+}_{(aq)} \quad (3)$$

This FeOOH is known to act as a catalyst for the ammonia oxidation reaction (AOR) under alkaline conditions, especially in Cu-containing systems.[52–54] In our system, FeOOH may adsorb ammonia and mediate a series of redox steps–including N–N coupling and dehydrogenation–releasing electrons as intermediates:

$$NH_{3(ads)} + OH^{-}_{(ads)} \rightarrow NH^{*}_{2(ads)} + H_2O + e^{-} \quad (4)$$

$$NH^{*}_{2(ads)} + NH_{3(aq)} + OH^{-}_{(ads)} \rightarrow N_2H^{*}_{4(ads)} + H_2O + e^{-} \quad (5)$$

These released electrons may then reduce Cu^{2+} to Cu^0, which nucleates as small nanoinclusions onto $CuWO_4$ particles–consistent with the formation of Cu^0 lattice fringes observed by HRTEM in Fe-treated samples. This hypothesis is strongly supported by our structural data, particularly: i) the absence of Cu^0 in pristine samples (lacking Fe); ii) the increased Cu^0 formation with higher Fe content; iii) and the confirmation that Fe is completely washed away post-treatment (Figures S16 and S17, Supporting Information). Moreover, XRD on pre-calcined Fe-treated samples (Figure S17, Supporting Information) shows early formation of WO_{3-x}, indicating that Fe-mediated phase segregation occurs already during hydrothermal treatment. Although iron was initially present in the powder post-hydrothermal treatment as FeOOH, it was likely converted into Fe_2O_3 during annealing and subsequently removed by HCl washing, confirming that iron did not incorporate into the $CuWO_4$ crystal lattice. This further supports the view that Fe^{3+} acts as a self-assembly mediator, rather than as a dopant or stable co-catalyst.

While spectroscopic and electrochemical data clearly indicate improved charge separation and interfacial dynamics in Fe-activated $CuWO_4$, one may question why the resulting photocurrents remain modest in absolute terms. A likely explanation lies in the morphological limitations of the thin-film architecture: the spray-coated films are composed of loosely packed particles, which are not interconnected and only partially in contact with the conductive FTO substrate. This restricts long-range charge extraction, even if local carrier separation is highly efficient. To isolate the intrinsic reactivity of the Fe-treated nanostructures—independent of film morphology—we performed a photocatalytic dye degradation test in aqueous dispersion using methylene blue (MB) under visible light (**Figure 6a**; Figure S15, Supporting Information). In this configuration, each nanoparticle acts as an independent suspended catalyst, with charge transfer occurring directly to molecular species in solution. Unlike in PEC testing, this process primarily probes the generation of reactive oxygen species (ROS) rather than interfacial water oxidation.

Both Fe-treated samples demonstrated significantly improved MB photodegradation compared to pristine $CuWO_4$, with Fe@$CuWO_4$ 0.8% achieving the highest removal efficiency. These results confirm that Fe activation enhances the particles' intrinsic photocatalytic activity, which we attribute to the formation of internal heterojunctions within each core–shell structure. The enhancement does not require macroscopic charge transport across a film, supporting the idea that performance in thin films is limited by poor connectivity rather than lack of material functionality. To further corroborate the formation of ROS, EPR spectroscopy in presence of a spin trap (DMPO, 5,5-Dimethyl-1-Pyrroline-*N*-Oxide) was employed under visible light irradiation. As shown in Figure 6b, the Fe-treated sample (Fe@$CuWO_4$) displayed a distinct quartet signal centered around B ≈ 3350 G (g ≈ 2.006), arising from the adduct formation between photogenerated hydroxyl radicals (•OH) and the spin trap.[55] In contrast, the pristine $CuWO_4$ showed negligible hydroxyl radical formation under identical conditions. This provides direct spectroscopic evidence that Fe-induced structural modification enhances ROS generation under light exposure. These findings reinforce our interpretation that the improved activity in photocatalysis arises from internal heterojunctions and defect sites that facilitate exciton separation and surface redox reactions.

The proposed mechanism is illustrated in Figure 6c. In pristine $CuWO_4$, photoinduced holes can in principle drive either the OER or ROS production (process A), but both are strongly limited by fast electron–hole recombination (process B) and trap-mediated losses associated with the material's indirect bandgap nature.[14] Additionally, the energy alignment hampers electron transfer toward the FTO substrate, as reflected in the negligible photocurrent under PEC conditions.

Upon Fe(III) activation, a hierarchical heterostructure forms within individual particles, featuring a crystalline $CuWO_4$ core surrounded by an amorphous WO_3-rich shell containing dispersed CuOx and metallic Cu domains. This architecture promotes localized pn junction formation, with p-type CuO[56] at the outer interface complementing the n-type $CuWO_4$ core. The resulting band bending favors hole extraction toward the electrolyte while reducing recombination losses. Although the shell is WO_3-rich, both morphological and spectroscopic data indicate that CuOx is preferentially located at the outermost surface, enabling efficient hole transfer to catalytically active CuO sites. This is consistent with prior studies on WO_3/$CuWO_4$/CuO systems[57] and corroborated by our ROS generation results in photocatalytic mode. These embedded heterojunctions enable directional charge separation at the single-particle level, even in the absence of extended electronic connectivity.

Moreover, WO_3 and metallic Cu domains act synergistically as electron sinks: WO_3 facilitates electron trapping via its low-lying conduction band, while metallic Cu inclusions serve as transient reservoirs or recombination barriers. These combined effects extend charge carrier lifetimes and improve interfacial transfer. As summarized in Figure 6c, the system supports two parallel activity modes: (A1) oxygen evolution at the solid–liquid interface via photogenerated holes under PEC conditions, and (A2) ROS generation in dispersion via electron–hole pairs under photocatalytic (PC) conditions. Both processes are enabled by the internal charge separation driven by the core–shell heterostructure. This Fe(III)-induced reorganization—achieved without co-catalyst decoration—offers a mechanistic explanation for the observed 30-fold photocurrent enhancement and dual PEC–PC functionality.

3. Conclusion

This work introduces a Fe(III)-mediated strategy to enhance the structural and functional properties of $CuWO_4$ nanostructures for both photoelectrochemical oxygen evolution and photocatalytic ROS generation. Rather than acting as a dopant or co-catalyst, Fe(III) transiently mediates a redox-driven self-assembly process, guiding the formation of a multiphase core–shell architecture composed of a crystalline $CuWO_4$ core, a partially amorphous CuO/WO_3 shell, and dispersed nanometric Cu^0-like inclusions. This configuration results in local pn junctions that facilitate efficient charge separation, reduce recombination, and establish catalytically active interfaces.

Fe-treated samples display a 30-fold photocurrent enhancement relative to pristine $CuWO_4$, as confirmed by LSV, Mott–Schottky, and IMPS analyses, without any change in electrochemical surface area—indicating that performance gains

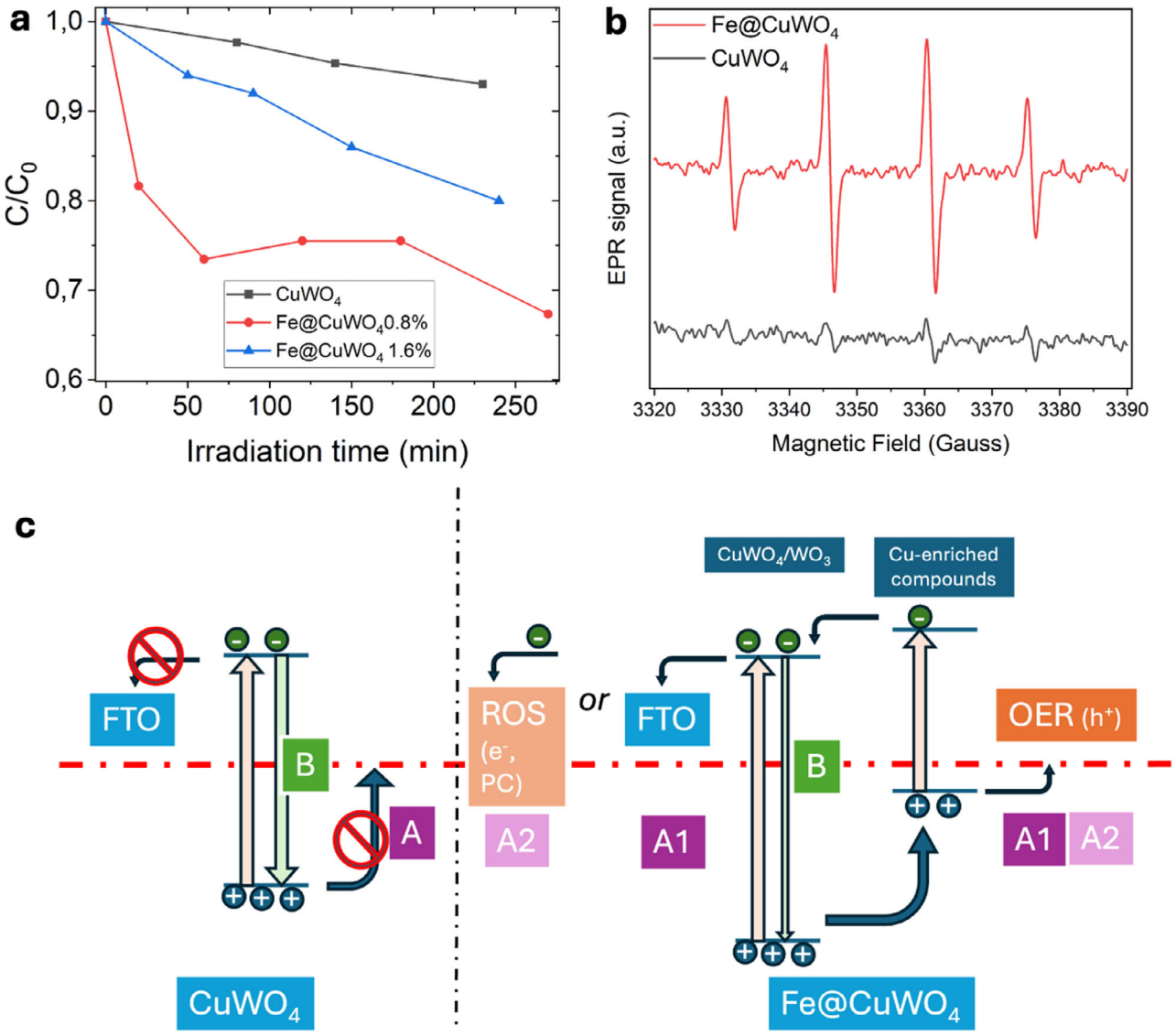

Figure 6. a) Photocatalytic degradation of MB under visible-light irradiation for pristine $CuWO_4$ and Fe-treated samples (0.8% and 1.6%). The enhanced degradation confirms increased reactive oxygen species (ROS) generation and validates the intrinsic catalytic activity of individual Fe@$CuWO_4$ particles in dispersion; b) EPR spectra of pristine and Fe-treated $CuWO_4$ samples under visible light irradiation in the presence of a spin-trapping agent. The Fe@$CuWO_4$ sample exhibits a characteristic multiline signal centered ≈ 335 mT, attributed to •OH, confirming the enhanced ROS generation induced by Fe-mediated structural reorganization; c) Schematic comparison of charge carrier behavior in pristine $CuWO_4$ and Fe-treated $CuWO_4$ (Fe@$CuWO_4$) particles under illumination. In pristine $CuWO_4$, photogenerated holes (A) may drive oxygen evolution reaction (OER), but the process is strongly hindered by electron–hole recombination (B), and by inefficient electron injection into FTO. In Fe@$CuWO_4$, the formation of a core–shell architecture with Cu-enriched domains and a WO_3-rich shell enables efficient charge separation. Photogenerated holes participate in both OER (A1) and ROS generation (A2) via parallel pathways, while electrons are funneled either toward the FTO contact (PEC mode) or retained in the particle for suspension-phase ROS production (PC mode). This synergistic mechanism accounts for the observed enhancement in both PEC and photocatalytic activity.

originate from intrinsic structural and electronic transformations. Complementary photocatalytic tests using methylene blue degradation and EPR detection of hydroxyl radicals demonstrate that individual Fe-activated particles function as effective ROS-generating units in dispersion, validating the dual applicability of the system as both a photoanode and a suspended photocatalyst.

Compositional analyses including ICP-OES revealed that Fe^{3+} concentrations in the final material are exceedingly low (≤0.076 at%) even when using nominal precursor concentrations up to 3.2 at%. These findings confirm that Fe(III) cannot be stably doped into the $CuWO_4$ lattice under the explored hydrothermal conditions—contrary to previous claims in the literature—and instead acts as a non-incorporating mediator that promotes phase segregation and nanostructure formation. This interpretation is consistent with recent hypotheses, including those proposed in the work of Lhermitte and Bartlett,[13] suggesting that the role of Fe may be misattributed in earlier studies.

Beyond its specific mechanistic contribution, this study underscores the importance of critically reassessing doping claims in transition metal oxides through robust analytical workflows. The use of high-sensitivity techniques such as ICP-OES, combined with thorough post-synthetic purification and control experiments, is essential to distinguish true substitutional doping from indirect structural effects.

The methodology presented here provides a new route for tailoring complex heterostructures in metal oxide photoelectrodes. Further investigations are warranted to explore the universality of this approach across different material systems. In particular, extending this strategy to more efficient photoanodes such as $BiVO_4$ or Ta_3N_5 could unlock new opportunities in phase control, defect engineering, and redox-mediated self-assembly for solar fuel applications.

4. Experimental Section

Chemicals: The following chemicals were employed in the present work: copper (II) nitrate trihydrate (98% purity, Sigma-Aldrich), ammonium metatungstate hydrate $(NH_4)_6H_2W_{12}O_{40}{\cdot}xH_2O$ (99% purity, Fluka), Hydrochloric acid (37% solution, Sigma-Aldrich), iron (III) nitrate nonahydrate $(Fe(NO_3)_3{\cdot}9H_2O$, 99.9% purity, Sigma-Aldrich) and ammmonia, NH_4OH (30% solution, 99.5% purity, Sigma-Aldrich). All chemicals were used as received, with no further purification.

$CuWO_4$ Synthesis Powder: $CuWO_4$ was obtained by subcritical hydrothermal synthesis followed by calcination. First, 5 mL of a 0.25 M ammonium metatungstate hydrate solution basified with ammonia (pH = 10) was added dropwise to 5 mL of a 0.25 M solution of $Cu(NO_3)_2{\cdot}3H_2O$ (resulting in a 1:1 molar ratio) and stirred. The mixture containing the precipitate formed was transferred to a Teflon-lined stainless-steel autoclave and heated in the oven at 180 °C for 24 h. The filling ratio is maintained at 1/2 of the total volume available. The autoclave was then left to cool to room temperature. A light-yellow precipitate was formed and recovered by centrifugation after several washing steps with distilled water and dried in the oven at 80 °C. This light-yellow powder was then calcined in air at 500 °C in a muffle furnace for 2 h. A grey-brown solid was recovered after complete cooling of the furnace, then washed with 0.5 M HCl, to remove excess unreacted Cu-based oxides, washed with methanol and distilled water and finally dried in an oven at 100 °C for future use and characterization.

Fe-Activated $CuWO_4$ Powder Synthesis: Fe-activated $CuWO_4$ samples were obtained using the above-described procedure, by adding different volume of a 0.01 M solution of iron (III) nitrate nonahydrate $(Fe(NO_3)_3{\cdot}9H_2O)$ to the mixture. The volume was adjusted so that the molar ratio Fe/Cu was 0.8 at% and 1.6 at%. Samples were named Fe@$CuWO_4$ 0.8% and Fe@$CuWO_4$ 1.6%, respectively.

Photoanode Development: The prepared powders were immobilized on the FTO substrate using the ultrasonic (US) spray coating method (ND-SP Ultrasonic Spray Coater, Nadetech Innovations, Spain), with a respective suspension of each material at a concentration of 0.5 g L^{-1} in isopropanol (IPA). Before the spraying process, the FTO glass was previously cleaned by sonication during 20 min, successively in soap, distilled water, acetone, isopropanol, and finally dried with a nitrogen air spray. FTO substrates underwent UVO cleaning for 20′ for improving film adhesion. The clean FTO glass was positioned at 8.6 mm distance from the nozzle on a hot plate previously set at 200 °C, and the suspension was sprayed at a 10 mL h^{-1} flow rate. Based on the desired thickness, different multilayer films were prepared (4, 8, 12, and 16 layers corresponding to 2.1, 4.2, 6.3, and 8.4 mL of suspension, respectively), where 8 layers architecture was determined to be the best choice according to PEC performances. The obtained films were then annealed at 300 °C for 1 h in air, to promote good adhesion with the substrate. After cooling to room temperature, the samples were ready to use.

UV–vis–NIR, Photoluminescence (PL) Characterization: The optical absorption spectra of the prepared $CuWO_4$ and Fe@$CuWO_4$ electrodes were recorded in absorption mode with a spectrophotometer (CARY 50 Probe UV–vis spectrophotometer). The baseline was recorded using clean FTO. The energy gap of the different photoanode were estimated using Cody plot method as described by Pei et al.[41] and detailed in the Supporting Methods. PL spectra on powder samples were measured by a fluorescence spectrophotometer FLS1000 (Edinburgh) using a 150 W Xe lamp as an excitation light source and the PMT980 photomultiplier (R13456P) as detector.

XPS, UPS: X-ray photoelectron spectroscopy (XPS) measurements were carried out through a Kratos Axis UltraDLD spectrometer (Kratos Analytical Ltd.) using a monochromated Al K_α X-ray source ($h\nu$ = 1486.6 eV) operated at 20 mA and 15 kV. High-resolution spectra were collected at a photoelectron pass energy of 20 eV and an energy step of 0.1 eV over an analysis area of 300 × 700 μm^2. The spectra were referenced to the adventitious carbon 1s peak at 284.8 eV. The spectra were analyzed with the CasaXPS software (Casa Software Ltd., version 2.3.24). The ultraviolet photoelectron spectroscopy (UPS) measurements were performed using a He I (21.22 eV) discharge lamp, fitted in the same chamber used for XPS analyses, on an area of 55 µm in diameter, at a pass energy of 10 eV and with a dwell time of 100 ms. The UPS spectra were referenced to the valence band maximum (VBM) measured via XPS extrapolating the primary edge cutoff (the lowest binding energy). The work function, i.e., the position of the Fermi level versus the vacuum level, was determined for each sample from the position of the secondary edge cutoff in the UPS spectrum (the highest binding energy).[58] A −9.0 V bias was applied to the sample to precisely determine the low-kinetic-energy cutoff.

Scanning Probe Microscopy Characterization: Atomic force microscopy (AFM) measurements were performed with an MFP 3D AFM by Asylum Research, in air at room temperature (RH < 35%) or in controlled dry chamber with RH<10% and moderate vacuum. During Kelvin probe microscopy (KPM) the AFM was mounting commercial probes (Bruker SCM-PIT). Topography and potential maps were acquired simultaneously, performing a second passage at a constant height after topography was acquired in the first pass. During the scan an ac voltage dithering was applied to the tip at a frequency close to its natural frequency. To avoid artifacts, trace and retrace data were always collected and compared. Raw data were processed with Gwyddion software, providing the surface roughness as root mean square value of irregularities (Sq). More details are present in the Supporting Information.

Scanning Electron Microscopy (SEM) and Energy-Dispersive X-Ray Analysis (EDX): SEM analysis was performed using a Zeiss GeminiSEM 560 (Zeiss, Oberkochen, Germany) field-emission gun operating at 1–5 kV acceleration voltage (1-2 kV for cross section, 5 kV for top view images). Secondary electrons detectors (SE2, InLens) were used to enhance the morphological differences between the samples. The microscope is coupled to an EDX detector (from Oxford Instruments, x-act PentaFET Precision) for X-rays microanalysis, working in energy dispersive mode, the EDX spectra were acquired at 20 kV.

Transmission Electron Microscopy (TEM): The morphology and microstructure of the samples were characterized by high resolution transmission electron microscopy (HR-TEM) and high-angle annular dark-field scanning transmission electron microscopy (HAADF-STEM) using a TEM JEOL F200 equipped with a cold-FE source. Elemental analysis and mapping were performed using a JEOL 100 mm^2 silicon drift energy dispersive X-ray spectrometer (EDX). A carbon supported gold grids, 400 mesh size, were used for preparation of the sample to avoid spurious copper signals in the EDX analysis.

Raman: A home-built setup was used to carry out Raman measurements. In brief, the excitation at 632.8 nm was provided by a continuous wave He-Ne laser (Melles Griot), coupled to a microscope (Olympia BX41) equipped with a 20x objective (Olympus LMPlan FLN 20× NA = 0.40). A three-stage subtractive spectrograph (S3000, Jobin Yvon) was used to separate the Raman from the Rayleigh scattering. The detector (Symphony, Jobin Yvon) was a liquid nitrogen cooled charge coupled device (CCD). The power impinging on the samples was 8 mW; spectra were recorded by integrating 20 seconds and averaging out of 30 acquisitions.

X-Ray Diffraction (XRD): XRD analysis was conducted using a PANalytical X'Pert diffractometer with Cu K_α radiation (λ = 1.54187 Å). Data acquisition utilized a 2D solid-state detector (PIXcel) over a range from 2θ = 10 to 60°, employing a step size of 0.013°. The crystalline phases in the XRD pattern were determined by the search and match procedure with the Bruker DiffracEVA software. The structures were subsequently refined with the Pawley-Rietveld method using the Bruker TOPAS software, by employing the COD 1008036, COD 1004057, and COD 1011148 for $CuWO_4$, WO_3, and CuO, respectively.

Photoelectrochemical (PEC) Tests: PEC tests were carried out in a 0.1 M KOH solution (pH 13.05) prepared by dissolving potassium hydroxide in MilliQ water. The measurements were conducted in a standard electrochemical cell. A Pt wire and Ag/AgCl electrode (0.212 V versus reference hydrogen electrode (RHE)) were used as counter and reference electrodes, respectively. Illumination was performed using a 100 mW cm^{-2} (neutral white, Philips LUMILEDS) light-emitting diode (LED) source controlled by the optical bench (Metrohm Autolab) coupled to the Autolab PGSTAT204 (Metrohm, Utrecht, The Netherlands) instrument. Incident Photon Conversion Efficiency (IPCE) tests were performed using LED sources (Philips LUMILEDS) with emission wavelengths at 470, 505, 530, 590, 617, 627, and 655 nm.

Intensity Modulated Photocurrent Spectroscopy (IMPS): IMPS analyses were carried out applying a LED frequency between 5000 and 1 Hz with a 15% of light intensity modulation. The white light intensity was set at 50 mW cm^{-2}. Electrochemical Impedance Spectroscopy (EIS) spectra were acquired from 100 mHz to 10 kHz with a potential modulation of 5 mV. Mott-Schottky plots were obtained recording EIS spectra between 0.8 and 1.4 V versus RHE, with 0.05 V steps. The capacitance values (C_P), was obtained by fittings with an equivalent circuit model (R(RQ)), while the flatband potential (V_{FB}) was measured by fitting the linear part of $1/Csc^2$ and finding the intercept with the voltage axis, using the Equation (6):[59]

$$\frac{1}{C_P^2} = \frac{2}{(\varepsilon_0 \varepsilon_r e N_D)} \left(V - V_{FB} - \frac{(K_B T)}{e} \right) \tag{6}$$

where C_P is the capacitance of the semiconductor ($1/{C_H}^2$, capacitance of the double layer, is considered negligible), ε_0 is the permittivity of free space, ε_r is relative permittivity of the target material, e is the electron charge (C), and k_B is the Boltzmann constant.

Furthermore, The IMPS response as a function of frequency can be expressed as:

$$j_{photo} = j_{hole} \frac{C_H}{C_H C_{SC}} + \frac{\left(k_{inj} + i\omega\right)}{\left(k_{rec} + k_{inj} + i\omega\right)} \left[\frac{1}{1 + i\omega\tau_c} \right] \tag{7}$$

where τ_C is the cell time constant, k_{rec} and k_{inj} are pseudo-first order rate constants for electron-hole recombination and charge injection (in the electrolyte), respectively, and j_{hole} is the photocurrent density before recombination. C_H and C_{SC} are the capacitances of the Helmholtz layer and the space charge region, respectively. Assuming that τ_C is at least two decades smaller than $\frac{1}{(k_{rec}+k_{inj})}$, two important numbers can be identified in the plot, i.e., the low frequency intercept (LFI):

$$LFI = \frac{C_H}{C_H + C_{SC}} \frac{\left(k_{inj}\right)}{\left(k_{inj} + k_{rec}\right)} \tag{8}$$

The high frequency intercept (HFI):

$$HFI = j_{hole} \frac{C_H}{C_H + C_{SC}} \tag{9}$$

Combining Equations (8) and (9), the ratio HFI/LFI corresponds to

$$\frac{k_{inj}}{k_{inj} + k_{rec}} \tag{10}$$

Thus, the maximum in the positive quadrant of the Nyqvist plot ($\omega_{max} = k_{inj} + k_{rec}$) is used for determining the rate constants. Mott-Schottky plot was realized according to the procedure reported in literature.[60]

Photocatalytic Degradation of Methylene Blue: Samples were prepared in duplicate in a 40 mL screw cap vial equipped with a stir bar. A methylene blue (MB) solution in MilliQ water (>18.3 MΩ cm) (40 mL, 4.42 mg L^{-1}, 0.012 mM MB) was adjusted at pH 6.97. The appropriate amount of catalyst (7.50 mg) was then added, and the mixture was left stirring in a foil-wrapped vial for 1 h at room temperature to allow for adsorption equilibrium between the dye and the catalyst. The vials were then illuminated using a homebuilt photoreactor made of white LEDs (Cree XLamp XT-E White LEDs, LEDsupply.com) with a light intensity of 280 mW cm^{-2} (measured using an Optical Power Meter PM100D with Optical Sensor S120VC from Thorlabs). Each vial was suspended on top of a LED and was continuously stirred at 400 rpm during the irradiation. After illumination, 0.6 mL of the mixture were removed from the vial and passed through a 13 mm syringe filter with 0.2 µm PTFE membrane before analysis by UV–vis spectroscopy. UV–vis absorption spectra in MilliQ water were recorded on an Shimadzu UV-2600i using a 1 cm quartz cuvette.

Electron Paramagnetic Resonance Spectroscopy (EPR): EPR spectra were recorded with a Bruker Elexsys580 spectrometer at X-band (9-10 GHz), using an ER4118X-MD5 dielectric ring resonator, inserted into an ER 4118CF cryostat for low-temperature measurements. All the conventional (continuous wave) spectra have been recorded at the temperature of 290 K or 80 K, using the following parameters: microwave power 1 mW, field modulation amplitude 1 Gauss, 4 scans. Pulsed EPR spectra (echo-detected EPR) were recorded using a $\pi/2$-τ-π-τ-echo microwave pulse sequence with and echo time τ of 200 ns and microwave pulses of 16–32 ns. For the spin trap experiments, 5,5-dimethyl-1-pyrroline *N*-oxide (25 mM DMPO, Merck 92688) was introduced together with the dispersed sample (1 mg mL^{-1}) and irradiated for 60 s, before measuring the EPR signal (20 mW microwave power and 0.028 mT modulation, 60 s sweep time) on a Bruker ESR5000 operating at a microwave frequency of 9.4 GHz.

Inductively Coupled Plasma – Optical Emission Spectroscopy (ICP-OES): Iron concentration in the powders was analyzed with a PerkinElmer Optima 4200 DV ICP-OES equipped with 2D CCD array; the plasma source is dual-view RFgenerator, i.e., it can be viewed both axially and radially. The calibration curve was performed before each series of analyses. Prior to analysis, the sample powders were accurately weighted and mineralized in a mixture of acid composed as follows: 1 mL HF (48% wt.), 2 mL HCl (37% wt.), 5 mL HNO_3 (69% wt.). The mixture has been heated at 100 °C for 2 h, until complete dissolution of the powders, then diluted to 50 mL with MilliQ Water and paper filtered.

Supporting Information

Supporting Information is available from the Wiley Online Library or from the author.

Acknowledgements

F.L. thanks the University of Padova for the financial support through the project "SOLARCUP P-DiSC # BIRD2024-UNIPD". M.W. and T.G. thank the financial support of Fondazione Compagnia di San Paolo for financial support through the "Bando TRAPEZIO—Paving the way to research excellence and talent attraction" and through the program "Attrazione e retention di docenti di qualità". F.L. and S.B. kindly acknowledge

Dr. Rosaria Brescia for SEM measurement management. L.Đ. gratefully thanks the support from the European Union (ERC, PhotoDark, 101077698).

Open access publishing facilitated by Universita degli Studi di Padova, as part of the Wiley - CRUI-CARE agreement.

Conflict of Interest

The authors declare no conflict of interest.

Data Availability Statement

The data that support the findings of this study are available from the corresponding author upon reasonable request.

Keywords

copper tungstate, defect engineering, heterojunctions, OER, self-assembly mediator

Received: July 2, 2025
Revised: August 2, 2025
Published online:

[1] T. Gatti, F. Lamberti, R. Mazzaro, I. Kriegel, D. Schlettwein, F. Enrichi, N. Lago, E. Di Maria, G. Meneghesso, A. Vomiero, S. Gross, *Adv. Energy Mater.* **2021**, *11*, 2101041.
[2] P. Dalle Feste, M. Crisci, F. Barbon, F. Tajoli, M. Salerno, F. Drago, M. Prato, S. Gross, T. Gatti, F. Lamberti, *Appl. Sci.* **2021**, *11*, 2016.
[3] D. Cheyns, B. Kam, K. Vasseur, P. Heremans, B. P. Rand, *J. Appl. Phys.* **2013**, *113*, 043109.
[4] M.-H. Park, J.-H. Li, A. Kumar, G. Li, Y. Yang, *Adv. Funct. Mater.* **2009**, *19*, 1241.
[5] Z. Wang, Y. Gu, L. Zheng, J. Hou, H. Zheng, S. Sun, L. Wang, *Adv. Mater.* **2022**, *34*, 2106776.
[6] Z. Qiu, Y. Ma, T. Edvinsson, *Nano Energy* **2019**, *66*, 104118.
[7] E. Kowalska, Z. Wei, M. Janczarek, *Visible Light-Active Photocatalysis*, Wiley, New York **2018**, p. 447–484.
[8] C. Ye, J. Liu, Q. Zhang, X. Jin, Y. Zhao, Z. Pan, G. Chen, Y. Qiu, D. Ye, L. Gu, G. I. N. Waterhouse, L. Guo, S. Yang, *J. Am. Chem. Soc.* **2021**, *143*, 14169.
[9] N. Li, D. K. Bediako, R. G. Hadt, D. Hayes, T. J. Kempa, F. von Cube, D. C. Bell, L. X. Chen, D. G. Nocera, *Proc. Natl. Acad. Sci.* **2017**, *114*, 1486.
[10] J. Zhang, Z. Zhao, Z. Xia, L. Dai, *Nat. Nanotechnol.* **2015**, *10*, 444.
[11] Y. Gao, T. W. Hamann, *J. Phys. Chem. Lett.* **2017**, *8*, 2700.
[12] D. Hu, P. Diao, D. Xu, M. Xia, Y. Gu, Q. Wu, C. Li, S. Yang, *Nanoscale* **2016**, *8*, 5892.
[13] C. R. Lhermitte, B. M. Bartlett, *Acc. Chem. Res.* **2016**, *49*, 1121.
[14] I. Grigioni, A. Polo, C. Nomellini, L. Vigni, A. Poma, M. V. Dozzi, E. Selli, *ACS Appl. Energy Mater.* **2023**, *6*, 10020.
[15] I. Grigioni, A. Polo, M. V. Dozzi, L. Ganzer, B. Bozzini, G. Cerullo, E. Selli, *J. Phys. Chem. C* **2021**, *125*, 5692.
[16] Y. Gao, T. W. Hamann, *Chem. Commun.* **2017**, *53*, 1285.
[17] P. Shadabipour, A. L. Raithel, T. W. Hamann, *ACS Appl. Mater. Interfaces* **2020**, *12*, 50592.
[18] J. E. Yourey, K. J. Pyper, J. B. Kurtz, B. M. Bartlett, *J. Phys. Chem. C* **2013**, *117*, 8708.
[19] C. Li, P. Diao, *Electrochim. Acta* **2020**, *352*, 136471.
[20] J. Yang, C. Li, P. Diao, *Electrochim. Acta* **2019**, *308*, 195.
[21] C. Nomellini, A. Polo, I. Grigioni, G. Marra, M. V. Dozzi, E. Selli, *Photochem. Photobiol. Sci.* **2023**, *22*, 2759.
[22] S. González-Poggini, B. Sánchez, M. Colet-Lagrille, *J. Electrochem. Soc.* **2023**, *170*, 066512.
[23] N. Le Minh Tri, D. Q. Trung, D. Van Thuan, N. T. Dieu Cam, T. Al Tahtamouni, T.-D. Pham, D. S. Duc, M. H. Thanh Tung, H. Van Ha, N. H. Anh Thu, H. T. Trang, *Int. J. Hydrogen Energy* **2020**, *45*, 18186.
[24] W. Chen, X. Pan, X. Bao, *J. Am. Chem. Soc.* **2007**, *129*, 7421.
[25] I. Volov, T. Saito, A. C. West, *J. Electrochem. Soc.* **2011**, *158*, D384.
[26] D. Bohra, W. A. Smith, *Phys. Chem. Chem. Phys.* **2015**, *17*, 9857.
[27] S. Yue, D. Fenqi, X. Donghang, D. Yang, Y. Jiao, L. Jia, H. Fan, Y. Sun, F. Du, D. Xie, D. Yang, Y. Jiao, L. Jia, H. Fan, *Chin. Phys. B* **2020**, *29*, 127801.
[28] Y. Kim, K. Broch, W. Lee, H. Ahn, J. Lee, D. Yoo, J. Kim, S. Chung, H. Sirringhaus, K. Kang, T. Lee, *Adv. Funct. Mater.* **2020**, *30*, 2000058.
[29] S. Gudjonsdottir, W. v. d. Stam, C. Koopman, B. Kwakkenbos, W. H. Evers, A. J. Houtepen, *Acs Appl. Nano Mater.* **2019**, *2*, 4900.
[30] R. K. R. Krishnan, S. Liu, D. Dahal, P. R. Paudel, B. Lüssem, *Adv. Opt. Mater.* **2021**, *9*, 1181109.
[31] Z. Shang, T. Heumueller, R. Prasanna, G. F. Burkhard, B. D. Naab, Z. Bao, M. D. McGehee, A. Salleo, *Adv. Energy Mater.* **2016**, *6*, 1601149.
[32] M. Davi, A. Drichel, M. Mann, T. Scholz, F. Schrader, A. Rokicinska, P. Kustrowski, R. Dronskowski, A. Slabon, *J. Phys. Chem. C* **2017**, *121*, 26265.
[33] L. Cai, J. Zhao, H. Li, J. Park, I. S. Cho, H. S. Han, X. Zheng, *ACS Energy Lett.* **2016**, *1*, 624.
[34] R. D. Shannon, *Acta Crystallogr., Sect. A: Found. Crystallogr.* **1976**, *32*, 751.
[35] I. Fontana, A. Lauria, G. Spinolo, *Phys. Status Solidi* **2007**, *244*, 4669.
[36] R. Dören, J. Hartmann, B. Leibauer, M. Panthöfer, M. Mondeshki, W. Tremel, *Dalt. Trans.* **2021**, *50*, 14027.
[37] R. Dören, B. Leibauer, M. A. Lange, E. Schechtel, L. Prädel, M. Panthöfer, M. Mondeshki, W. Tremel, *Nanoscale* **2021**, *13*, 8146.
[38] X. Guo, X. Qin, Z. Xue, C. Zhang, X. Sun, J. Hou, T. Wang, *RSC Adv.* **2016**, *6*, 48537.
[39] L. Pirker, B. Višić, J. Kovač, S. D. Škapin, M. Remškar, *Nanomaterials* **2021**, *11*, 1985.
[40] Z. Huang, J. Song, L. Pan, X. Zhang, L. Wang, J. Zou, *Adv. Mater.* **2015**, *27*, 5309.
[41] P. Liu, P. Longo, A. Zaslavsky, D. Pacifici, *J. Appl. Phys.* **2016**, *119*, 014304.
[42] E. L. S. Souza, J. C. Sczancoski, I. C. Nogueira, M. A. P. Almeida, M. O. Orlandi, M. S. Li, R. A. S. Luz, M. G. R. Filho, E. Longo, L. S. Cavalcante, *Ultrason. Sonochem.* **2017**, *38*, 256.
[43] J. E. Yourey, B. M. Bartlett, *J. Mater. Chem.* **2011**, *21*, 7651.
[44] X. Duan, C. Xu, A. M. El Nahrawy, J. Chen, Z. Zhu, J. Wang, Q. Liang, F. Cao, *ChemNanoMat* **2022**, *8*, 202100419.
[45] Z. Zhang, C. Xiao, S. Li, *Mater. Lett.* **2018**, *232*, 25.
[46] M. Nolan, S. D. Elliott, *Phys. Chem. Chem. Phys.* **2006**, *8*, 5350.
[47] F. Zhan, G. Wen, R. Li, C. Feng, Y. Liu, Y. Liu, M. Zhu, Y. Zheng, Y. Zhao, P. La, *Phys. Chem. Chem. Phys.* **2024**, *26*, 11182.
[48] M. Drosou, C. A. Mitsopoulou, M. Orio, D. A. Pantazis, *Magnetochemistry* **2022**, *8*, 36.
[49] A. Goswami, D. Ghosh, V. V. Chernyshev, A. Dey, D. Pradhan, K. Biradha, *ACS Appl. Mater. Interfaces* **2020**, *12*, 33679.
[50] K. Gelderman, L. Lee, S. W. Donne, *J. Chem. Educ.* **2007**, *84*, 685.
[51] S. Krehula, S. Popović, S. Musić, *Mater. Lett.* **2002**, *54*, 108.
[52] S. Zhang, H. Jiang, L. Yan, Y. Zhao, L. Yang, Q. Fu, D. Li, J. Zhang, X. Zhao, *Small* **2023**, *19*, 2005616.
[53] M. Kuang, Q. Wang, H. Ge, P. Han, Z. Gu, A. M. Al-Enizi, G. Zheng, *ACS Energy Lett.* **2017**, *2*, 2498.

[54] M. Zhu, Y. Yang, S. Xi, C. Diao, Z. Yu, W. S. V. Lee, J. Xue, *Small* **2021**, *17*, 2005616.
[55] E. Finkelstein, G. M. Rosen, E. J. Rauckman, *Arch. Biochem. Biophys.* **1980**, *200*, 1.
[56] D. Wu, Q. Zhang, M. Tao, *Phys. Rev. B* **2006**, *73*, 235206.
[57] J. Li, S. Hu, S. Liu, S. Hou, L. Li, J. Huang, *Int. J. Hydrogen Energy* **2024**, *61*, 967.
[58] Q. A. Akkerman, M. Gandini, F. Di Stasio, P. Rastogi, F. Palazon, G. Bertoni, J. M. Ball, M. Prato, A. Petrozza, L. Manna, *Nat. Energy* **2016**, *2*, 16194.
[59] B. Klahr, S. Gimenez, F. Fabregat-Santiago, T. Hamann, J. Bisquert, *J. Am. Chem. Soc.* **2012**, *134*, 4294.
[60] A. J. Bard, L. R. Faulkner, *Electrochemical Methods: Fundamentals and Applications*, 2nd ed., Wiley, New York, NY, **2001**.